Cross-Borehole Compressional Wave Imaging of Unconsolidated Sediments

TIMOTHY H. LARKIN, PAUL A. JOHNSON, PAUL M. RICH, GREG EISCHEID, AND W. SCOTT PHILLIPS

***Abstract*—Cross-borehole elastic wave tomography offers great potential for nondestructive imaging of near-surface sediments, fluids, and soils. Using this method, we created a high-resolution tomographic image of velocity structure from simulated sedimentary layers obtained using compressional wave travel times. The image shows three distinct layers and a water-filled container located in the center of the middle layer. An image obtained from computer simulated travel times shows good agreement with the image from laboratory data. The high-quality data and resulting image were due in part to a novel transmitter and receiver design. These were composed of cylindrical piezoelectric transducers individually sealed in oil-filled Teflon containers and stacked to form stringers. The transmitters were extremely efficient at coupling energy into the medium. The transmitter frequency was 135 kHz, velocities ranged from 1.4 to 1.8 km/s, and thus wavelengths were 1.0–1.4 cm. The distance between boreholes was 30 cm, with about 60 cm of vertical coverage.**

I. Introduction

UNDERSTANDING subsurface ecological and hydrological processes is limited by the lack of noninvasive field tools. Current methods for the detailed field study of sediments, fluids, soils, and plant roots generally require destructive sampling by coring or excavation. Our research has focused on laboratory development and testing of cross-borehole elastic wave tomography. Our goal is to develop tools and methods that can be used for high-resolution *in situ* imaging of sediments and soils. (We use the terms "imaging" and "tomographic reconstruction" synonymously.)

Surficial sediments and soils are extremely dissipative to elastic wave energy, much more so than most rocks that have a rigid matrix. Thus, imaging these materials presents a difficult challenge, especially since we are interested in small-scale inhomogeneities that require using high frequencies. High frequencies attenuate more than lower frequencies over comparable propagation distances. In this study, we image layers composed of saturated quartzo-feldspathic and clay-rich quartz sands. Saturated sands tend to attenuate elastic wave energy less than soils, clays, and undersaturated media, and thus imaging them is an appropriate first step toward our goal. By imaging moderately dissipative materials such as saturated sands, we are a step closer to working with media that are extremely attenuating to elastic wave energy such as clays, soils, and undersaturated materials.

This paper describes two phases in our most recent studies. First, we determined compressional wave velocity, attenuation, and transmission characteristics in two test sands. Second, we conducted an imaging experiment in layered sands, with an embedded low-velocity zone. We evaluated the imaging results by comparing them to results obtained using computer-simulated travel times.

Manuscript received August 3, 1989; revised March 29, 1990. This work was performed under the auspices of the U.S. Department of Energy's National Environmental Research Park Program under Contract W-7405-ENG-36 with Los Alamos National Laboratory.

The authors are with the Los Alamos National Laboratory, Mail Stop D443, Los Alamos, NM 87545.

IEEE Log Number 9037454.

II. Background

A. Other Techniques Demonstrating Potential for Remote Sensing of Sediments and Soils

Many geophysical methods offer the possibility of high-resolution imaging in sediments and soils. Various methods measure different physical properties. For example, gravity is sensitive to density, magnetics to magnetic susceptibility, electromagnetic (EM) waves to electrical conductivity, radar to dielectric constant, while elastic waves are sensitive to velocity and density [1], [2]. Ultimately, a combination of methods will more than likely be most useful. Toward that end, we are currently studying how to use compressional waves to image unconsolidated sediments and soils.

In laboratory and small-scale field studies, only a few methods are currently being developed to image sediments, soils, fluids, and roots. X-ray [3] and nuclear magnetic resonance [4] techniques offer promise for use in imaging these media under laboratory conditions; however, as field tools, these methods are not currently practical. Of the various EM techniques, only ground-penetrating radar is being tested for potential field use in high-resolution subsurface remote imaging.

Of the eleastic wave methods, the cross-borehole technique is the most effective in terms of wave attenuation and geometry. Elastic waves attenuate dramatically in sediments and soils. Because reflection and refraction techniques are surface based, they require two-way travel of waves from the surface to an interface and back to the surface. In contrast, the cross-borehole method uses direct transmission between transmitters and receivers located in adjacent boreholes. Therefore the effect of atten-

0196-2892/90/0900-0922$01.00

uation is reduced because only one-way ray paths are required. Additionally, the cross-borehole geometry is more amenable to tomographic reconstruction because of the diversity of possible ray paths, and thus the high degree of coverage.

B. The Cross-Borehole Elastic Wave Method

In the cross-borehole method, a transmitter excites a signal in one borehole, and this signal is received in an adjacent borehole. Commonly, the receiver is then moved some predetermined distance vertically, and the procedure is repeated until many different ray paths are collected for a single transmitter position. The transmitter is then moved a short distance vertically and the entire procedure is repeated. This operation is repeated until a sufficiently large number of criss-crossing ray paths have been collected through the medium of interest. The travel times of the collected signals are then used to image the velocity structure of the medium through which the signals pass.

Cross-borehole techniques have been used successfully to determine *in situ* properties of crystalline and sedimentary rock. Early studies were performed by workers interested in the behavior of elastic waves in rock [5], [6]. Investigations of material layering and anisotropy were carried out using the cross-borehole technique [7]. Since then, the cross-borehole technique has been used to help solve various civil engineering problems [8], [9], including studies of properties of San Francisco Bay sediments for earthquake engineering purposes [10] and for siting the Trans-Bay Tube [11].

Reconstruction of two-dimensional subsurface structures by computerized tomography began in the 1970's, drawing from the original development of tomography in the medical field (e.g., "CAT" scans [12], [13]). Tomography is the inversion process through which data collected on a boundary are used to estimate the distribution of physical properties of the enclosed area or volume. Interest in characterizing the host environment of petroleum [14], coal [15], iron ore deposits [16], geothermal reservoirs [17], and enhanced oil recovery [18] has drawn earth scientists to cross-borehole elastic wave tomography. Cross-borehole tomography has also been applied to the detection of fractures in crystalline rock [19], and to the characterization of changes in rock properties resulting from heating by radioactive waste canisters [20]. The Swiss National Cooperative for Storage of Radioactive Waste (NAGRA) has used cross-borehole techniques in comprehensive characterization of granitic rock for radioactive waste storage [21]. A comparison of various tomographic reconstruction schemes has been provided by Peterson *et al.* [22], and computational aspects of the problem have been discussed by McMechan [23], Menke [24], Ramirez [25], Ivansson [26], and Phillips *et al.* [27].

C. Experimental Design and Techniques

We conducted experiments in two areas leading up to the imaging experiment. These areas included improving transmitter and receiver design, and media characterization experiments. The transducer design experiments were aimed at improving the signal quality. Media characterization experiments were conducted to aid in the evaluation of the tomography results.

D. Transmitter/Receiver Design

Constructing transmitters and receivers that operate effectively in cross-borehole experiments is difficult. Among other problems, sources tend to excite tube waves or guided waves that propagate upward and downward in the source borehole, rather than compressional waves [28]. We found the following design effective at coupling compressional waves in and out of the sand, while avoiding tube waves. Cylindrical, lead-zirconate–titanate (PZT), piezoelectric transducers were used for both transmitters and receivers (Fig. 1). Cylindrical transducers performed much better than disk-shaped and pin-shaped transducers as far as signal amplitude for a given input voltage is concerned. Each transducer was placed inside a Teflon container filled with silicon oil. Tests with a variety of plastic and metal container materials showed that Teflon had the best transmission and reception properties when comparing input voltages to received signals. Teflon containers were threaded at both ends so that each container could be attached to other identical containers. Each receiver transducer was centered within its individual container and allowed to resonate freely radially. Each transmitter transducer was also centered and mechanically damped slightly to prevent continued resonance after being excited by the transmitted signal. Damping was accomplished by mechanically restricting movement about a centralizing support. Continued resonance of the transmitter is a cause of noise; however, allowing the receiver to resonate makes it more sensitive. Damping the transmitter while not damping the receiver improved the signal-to-noise ratio.

We stacked eight transducers to form a transmitter stringer, and another eight transducers to form a receiver stringer. Thus, signals from 64 ray paths could be collected without moving either stringer, minimizing disruption of the sands. Movement of the stringers was hand controlled using Plexiglas pipes fitted to both ends of the stringers and supported by guides at the container top and bottom. The guides allowed us to measure vertical displacements precisely and to minimize horizontal distance uncertainties by restricting lateral movement.

Each transducer container was wired so that transducers could be excited independently. Wires exited through small holes on the side of each container and were guided to the surface on the outside of the stringers. Holes were placed above each transducer, rather than on the sides, to prevent interference with transmission or reception. Wires were located on the side of the stringers away from the region to be imaged. RTV sealant was used to seal holes. The transmitter stringer and wires were wrapped in aluminum foil for shielding against EM noise. Both transmitter and receiver stringers were then encased in heat-

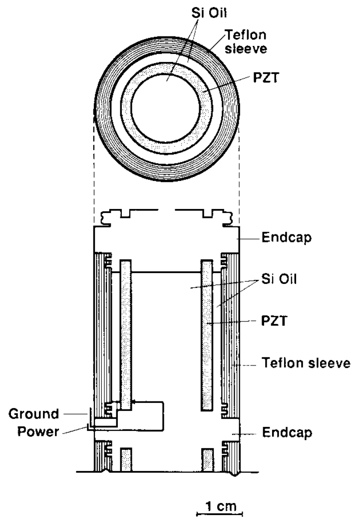

Fig. 1. Piezoelectric transducer design.

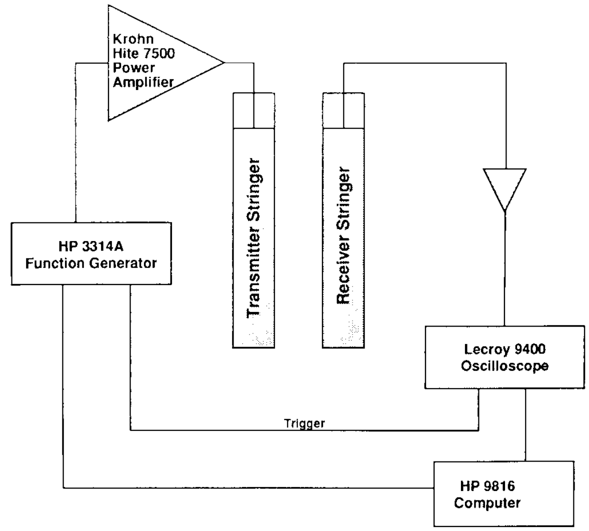

Fig. 2. Block diagram of experimental configuration.

shrink tubing to protect wiring and foil from abrasion during stringer movement.

We found that using slightly larger transmitters than receivers enhanced the signal-to-noise ratio. The different sizes of transducers correspond to different peak responses. The transmitter and receiver transducers we chose had center frequency responses of 40 and 100 kHz, respectively, and were manufactured by Channel Industries, Inc. The diameters of the transmitter and receiver transducers were 2.54 and 1.06 cm, respectively. The vertical distance between transducers center-to-center in the transmitter and receiver stringers was 5.50 and 3.30 cm, respectively. The stringers could be located within a vertical error of less than 1 mm.

E. Experimental Configuration

Fig. 2 shows a schematic diagram of the experimental configuration. A Hewlett–Packard 9920 function generator supplied a single sine-wave cycle that was amplified by a Krohn–Hite power amplifier. The signal was transmitted by one of the transducers in the transmitter stringer, detected at a single receiver, and relayed through a preamplifier to a LeCroy 9400 digital oscilloscope. Travel times were read from the waveform recorder using cursors at high vertical gain, and signals were then sent to an HP 9816 computer for storage and plotting. The computer controlled the actual imaging experiment and all associated apparatus.

F. Preliminary Experiments on Individual Sands

Preliminary experiments were conducted to characterize the seismic quality factor Q (inversely proportional to attenuation) and the compressional wave velocity in the two sands. We chose two sands to study. The first was a concrete-grade, quartzo-feldspathic sand containing 5% other minerals, mostly biotite (hereafter termed "concrete sand") with grain sizes on the order of 0.5–2 mm. The second material was a clay rich, silty-sand with grain sizes of 0.1–1 mm, obtained from the banks of the Rio Grande (hereafter termed "RG sand").

Attenuation was measured in each sand using the spectral ratio method [29]. Measurements of the amplitudes of pulsed arrivals at four transmitter/receiver distances were made at a frequency of 135 kHz. Velocities were calculated from the measured travel times of the first arriving compressional wave assuming straight ray paths. These measurements were obtained at a depth of approximately 10 cm. With the addition of overburden in the imaging experiment, these velocities would be expected to increase several percent. One sine-wave cycle was input from the function generator into the transmitter for both the amplitude and velocity measurements.

G. Tomography Experiment

After characterizing the transmission properties, we conducted a tomographic reconstruction experiment to determine our ability to detect subsurface velocity heterogeneity. The tomography experiment was conducted inside a plastic barrel measuring approximately 90 cm high by 61 cm wide. Fig. 3 shows a schematic diagram of the setup. We used the two sands characterized in the above experiments for the tomography experiment. The area imaged was composed of three layers: the RG sand was used for the top and bottom layers, and the concrete sand was used for the middle layer. All layers were 100% water saturated. Water was added through a valve from the barrel bottom; adding water from below forced air to the surface. Gravel was used as the lowermost layer in the barrel to distribute water evenly at the base. Once all the layers were saturated, the water was cycled out of and back into

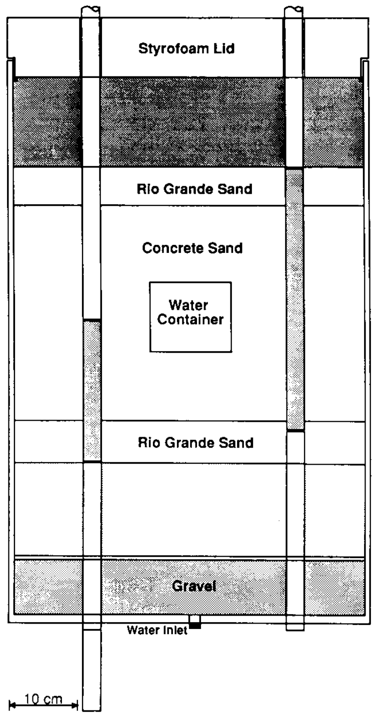

Fig. 3. Geometrical relationships within test container.

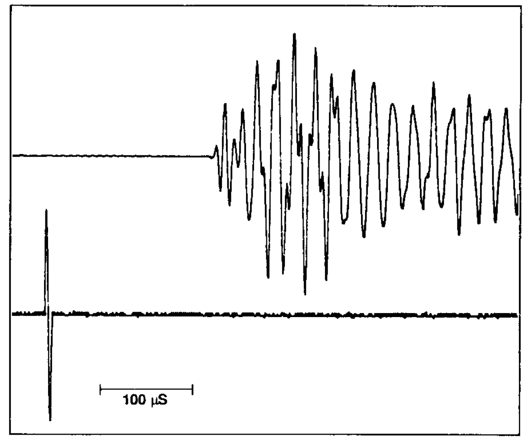

Fig. 4. Typical received signal (top) and transmitter pulse from the function generator (bottom).

the layers several times. In this manner, we were able to compact the sands and force out virtually all air.

A 10 × 10 × 10 cm water-filled container was buried in the center of the middle layer. The container was made of supple plastic with walls 0.2 mm thick. The water container was used to see if we could distinguish between saturated sand and water. A 17 cm layer of concrete sand was placed above the uppermost layer to add lithostatic pressure, compacting the layers, and thereby enhancing elastic wave coupling. Plastic film several microns thick was placed between each layer to inhibit layer mixing, and thereby produce sharp boundaries. The plastic film was perforated so that water passage was not blocked. The region to be imaged was located in the center of the barrel; thus, sidewall reflections arrived well behind the first arriving compressional wave and did not interfere with travel time interpretations (Fig. 3). Once the layers were in place and water cycling was complete, the barrel was left standing for several days for further consolidation so that little or no change would take place during the experiment.

A single 135 kHz, 80 V pulse was used to excite the transmitter at a repetition rate of 10 ms. Received signals were summation averaged a minimum of 100 times and up to several thousand times, depending on the signal-to-noise ratio. Travel times were visually determined from the expanded scales available on the waveform recorder. An example of the signal used to excite the transmitter is shown in Fig. 4, along with a received signal.

Each observation was assigned a quality rating. The ratings were as follows:

1) first arrival not detectable;
2) poor first arrival, signal very emergent;
3) good first arrival, but signal somewhat emergent;
4) excellent first arrival, but signal slightly emergent; and
5) excellent first arrival.

Emergent describes arrivals that gradually increase in amplitude with time. Quality ratings were later used to discard poor travel time determinations before imaging.

Data collection took place as follows. A transmitter was excited for each receiver as shown in Fig. 5. Likewise, the next transmitter was excited for all receivers. This process was repeated until 64 signals were collected from all possible combinations of transmitters and receivers. After these 64 signals had been collected, the transmitter stringer was moved downward, and another 64 signals were collected. The receiver stringer was then moved downward, and again the collection procedure was repeated. In this manner, we collected 960 signals through the layered region. The angle between transmitter and receivers ranged from +50° to −50° as measured from horizontal.

H. Tomography Algorithm

The iterative back-projection method we use for obtaining a velocity tomograph from observed compressional wave travel times is as follows. The interborehole region is divided into a number of discrete pixels. Initially, each pixel is assigned velocity, based on an educated estimate. For example, one of the layer velocities may be assigned to the entire region for the initial estimate. Travel times from rays traversing the matrix of slowness pixels are then generated, allowing the calculation of the travel time residual. The residual represents the difference between the observed travel time and the computer-generated travel time from a ray passing through the matrix of pixels. Based on the travel time residual, each pixel velocity is

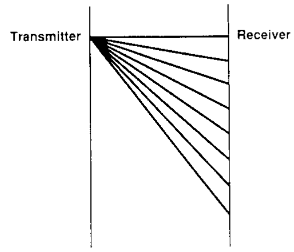

Fig. 5. Schematic showing straight ray paths of a single data scan.

adjusted to minimize the residual. This procedure is performed for all ray paths, and is then repeated until the computer-generated travel times are approximately equal to the observed travel times, in which case the residuals reach some reasonably small value.

The method described above belongs to a class of methods known as iterative back-projection. Specifically, we used the minimum energy technique as described by Dines and Lytle [30]. For a given ray path and associated travel time residual Δt_r, the slowness correction, or inverse of velocity, applied to pixel p is

$$\Delta s_p = \frac{l_{rp}\,\Delta t_r}{\sum_i l_{ri}^2}$$

where l_{rp} is the path length of ray r within pixel p, and the sum is performed over all pixels within the computer model.

For a given iteration, the slowness corrections may be applied after each ray is considered (algebraic reconstruction, ART [13], [22]) or averaged and applied after all rays are considered (simultaneous iterative reconstruction, SIRT). SIRT is generally thought to perform better than ART in cases where poorly determined travel times are present; experience with geophysical data sets has convinced us that SIRT is more effective [27].

To simplify the calculations, we assumed straight ray paths. This is equivalent to assuming that only small fluctuations exist in the true velocity model, such that refraction effects can be ignored. Dines and Lytle [30] were able to apply straight ray techniques successfully in cases where the velocity fluctuation was 16%. We expect a maximum of 20% velocity variation based on our preliminary experiments. Therefore the velocities are such that bending rays may improve inversion results.

Our method also includes an optional two-dimensional smoothing algorithm of arbitrary size and shape that operates between the back-projection iterations and helps to remove any model oscillations of such small scale to be deemed unrealistic.

To establish the quality of the tomographic reconstruction from observed travel times, a computer-generated tomograph was created using model data for comparison to the real data result. Computer-generated ray paths and corresponding travel times were obtained using a model of the imaged region. These data were then inverted to create a tomograph of "perfect data."

III. Results

A. Results from Individual Sands

Results of velocity and attenuation for individual sands are summarized in Table I. This table shows compressional wave velocity and the quality factor Q at 100% water saturation for the two sands used in the tomography experiments. The average compressional wave velocity in the concrete sand, 1.80 km/s, is 20% higher than that in RG sand, 1.44 km/s. The water velocity is 1.50 km/s. The Q measurement is also higher in the concrete sand than the RG sand: 25 versus 11.

B. Tomography Experiment

Collecting 960 ray paths through the region of study required 8 days.[1] The first two data scans were repeated after the completion of the experiment to test whether or not further compaction had affected the observations over the duration of the experiment. The observed travel times matched within the accuracy of our measurements. Travel time observation error (accuracy) was approximately 2 μs (1.2% of total travel time), and the estimated precision was 1 μs (0.6%). The accuracy was estimated from the travel time error due to the emergence of signals. The precision was determined from repeated observations of a single travel time.

A representative data scan is shown in Fig. 6. The hyperbolic travel time change of rays traversing increasing angles from horizontal is clearly seen. Based on the signal-to-noise ratio, the overall data quality is very good. Table II summarizes the quality of the received signals. Most travel time observations were of excellent quality, either 4 or 5.

A plot of signals from only horizontal ray paths is shown at the right in Fig. 7, together with a schematic of the experimental geometry at the left. This figure shows velocity variations between the different layers. Note the first arrivals of signals corresponding to the RG sand at the top and bottom of the plot. These travel times are markedly lower (approximately 6%) than those in the concrete sand. Paths that include concrete sand and the water container are also relatively slow (approximately 4%) as compared to the pure concrete sand paths. The accuracy of the travel time measurements is considerably better than the travel time variations between media.

Fig. 8(a) shows "apparent" velocities calculated from the 660 compressional wave travel time determinations used in the travel time inversion, and Fig. 8(b) shows the "apparent" velocities from perfect data. The velocities are "apparent" rather than "true" velocities because we assume straight ray paths. The vertical axis corresponds

[1] Note that increasing the rate of data collection is a simple matter. Using a recorder with many data collection channels and a computer algorithm for automatic travel time determinations could allow an experiment to be conducted in minutes.

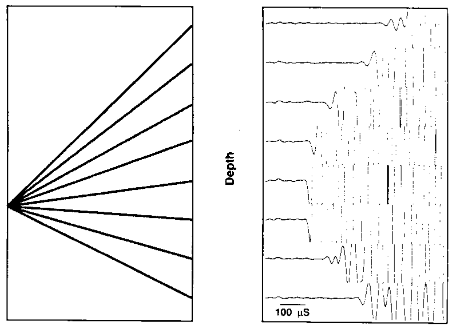

Fig. 6. Typical data scan collected between transmitter and receiver stringers in the sediments.

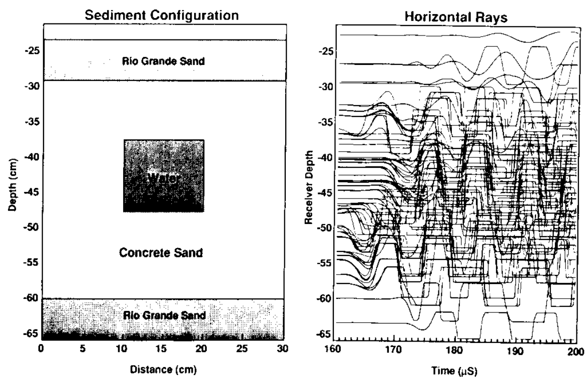

(a) (b)

Fig. 7 (a) Layered sediment geometry. (b) Received signals for horizontal ray paths through region in (a). Most first arrivals are very clear. The amplitudes of wavetrains following the first arrivals are nearly all saturated; the instrument did not have the vertical resolution to collect all of the signal. This is because we were maximizing amplitudes of the first arrivals to facilitate travel time determinations. Real amplitudes vary from trace to trace and were scaled manually.

TABLE I
MEDIA PROPERTIES AT COMPLETE SATURATION

Material	Average Velocity (km/s)	Quality Factor (Dimensionless)
Concrete Sand	1.80	25
Rio Grande Sand	1.44	11
Water	1.50	

TABLE II
TRAVEL TIME QUALITY RANKING VERSUS FREQUENCY OF OCCURRENCE

Quality	Number of Signals
5	665
4	141
3	87
2	32
1	35

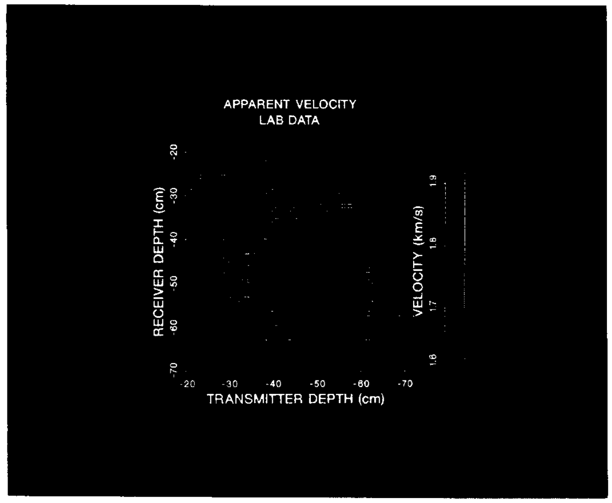

(a)

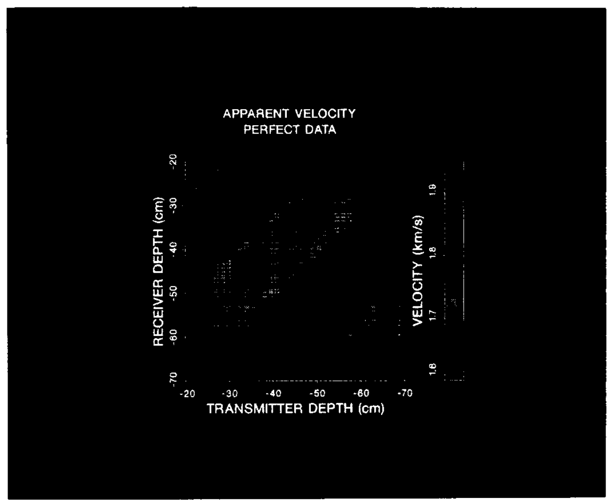

(b)

Fig. 8. (a) Apparent velocities of laboratory data, and (b) apparent velocities of perfect data. Transmitter depths are shown on the vertical axis, and receiver depths are shown on the horizontal axis. Apparent velocities are shown on the color bar at right in km/s. See text for explanation of velocity variations.

to receiver depths, and the horizontal axis corresponds to transmitter depths. Cooler colors represent faster velocities, and warmer colors represent slower velocities, as indicated by the color bar. The diagonal from the top left to the bottom right in the figures represents horizontal ray velocities. The low-velocity region oriented top right to bottom left corresponds to the water container. This is clearly visible in the perfect data as a yellow region. In the laboratory data, the water container effect is shown as a green and yellow region, although it is less clear than in the perfect data plot. The surrounding faster velocities on either side of the water container correspond to the concrete sand. The lower velocities at the top left and bottom right correspond to rays that have travelled through

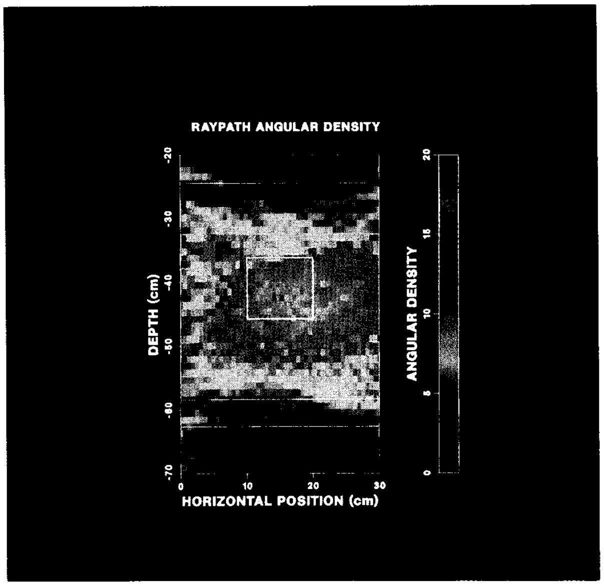

Fig. 9. Ray path angular density with number of angles per pixel shown on color bar at right. Overlay of the experimental geometry shown in black.

the RG sand. Regions where there are no data, mostly in the top left and bottom right of the figure, correspond to the longest travel paths and most extreme angles between transmitters and receivers. For the most part, these data were discarded because of their poor quality. Elsewhere, some observations are missing because they were of qualities 1–3.

The quality of the tomographic inversion is dependent on the number of ray paths and the distribution of angles of rays which pass through each pixel [24], [25]. That is, a large number of ray paths passing through a given pixel at many orientations produces a better estimate of the velocity through that pixel. Fig. 9 shows the number of different ray path angles through each pixel in relation to the experimental geometry. The ray path angle density plot was generated by dividing the aperture of ray path coverage ($\pm 50°$) into 4° bins for each pixel. These bins were assigned either 1 or 0 for each data bin, depending on whether or not any rays fell within the angular limits of that bin. Numbers assigned to bins were then summed for each pixel. There are 50×50 pixels shown. The warmer colors in this figure represent larger numbers of ray path angles per pixel. From Fig. 9, it is clear there is a larger number of ray path angles in the region corresponding to the water container, as delineated by the black outline.

The travel time data shown in Fig. 8(a) were used in the inversion to compute the velocity tomograph shown in Fig. 10(a). Fig. 10(b) and (c) shows travel time inversion results from the perfect data and from perfect data with noise, respectively. In the case of perfect data with noise, Gaussian noise with a standard deviation of 1.7 μs (1.0% of the total travel time) was added to simulate real data. The amount of noise added to the perfect data was based on the rms travel time error between the real and model data (1.26 μs) and the estimated travel time error (2.0 μs). A 50×50 matrix of pixels was used in the inversions, and the images shown were produced with 12 iterations. Again, cooler colors represent faster velocities and warmer colors represent slower velocities. From the laboratory data tomograph, the approximate velocity range of the concrete sand is between 1.85–1.90 km/s, for the RG sand, the range is 1.65–1.70 km/s, and for the water the range is 1.7–1.8 km/s. All of these velocities are faster than actual measured velocities (compare Table I).

Smoothing was performed between iterations by averaging eight adjacent pixel slownesses together at a time. Smoothing removes unrealistic pixel-to-pixel velocity oscillations that commonly occur.

IV. Discussion

A. Preliminary Experiments

The results of the preliminary experiments show that there are distinct velocity differences between the two sands. The differences in velocity between the concrete sand and RG sand can be attributed to the clay within the RG sand. The compressional wave velocity in the RG sand is less because of its partial clay content; the clay content in pore spaces generally decreases velocity [31]. In addition, the quality factor may be smaller in the RG sand because of its clay content [32]. The physical property differences between materials are important because they indicate we should detect meaningful physical characteristics in the imaging experiment.

B. Tomography Experiment

The plots of apparent velocities are similar for laboratory and perfect data, respectively (shown in Fig. 8(a) and (b)). That is, the effects of all three layers and the water container can be seen in both plots. The laboratory data plot, however, displays considerably more noise than the perfect data because of errors in travel time determinations.

In the inversion image, the lower boundary of the concrete sand is distinct, except for the high-velocity region just to the right of the center in the layer, as can be seen by comparing the inversion of lab data to the geometry of the imaged region in Fig. 10(a). This higher velocity is due to one or more early travel time determinations from rays passing at steep angles through this region. The lower boundary of the top RG layer is irregular due to the overall poorer travel time determinations in this region, ray bending artifacts, and to inversion artifacts (the low velocities below the layer on either side of the plot). The low-velocity zone corresponding to the water container is distinct. The container appears in green at the center of

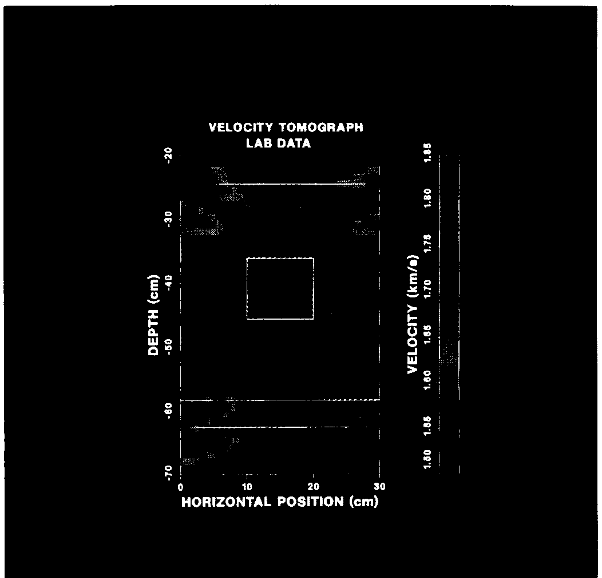

(a)

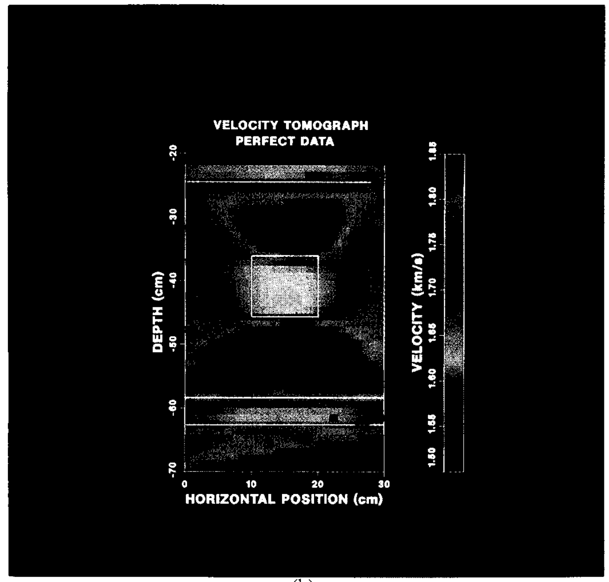

(b)

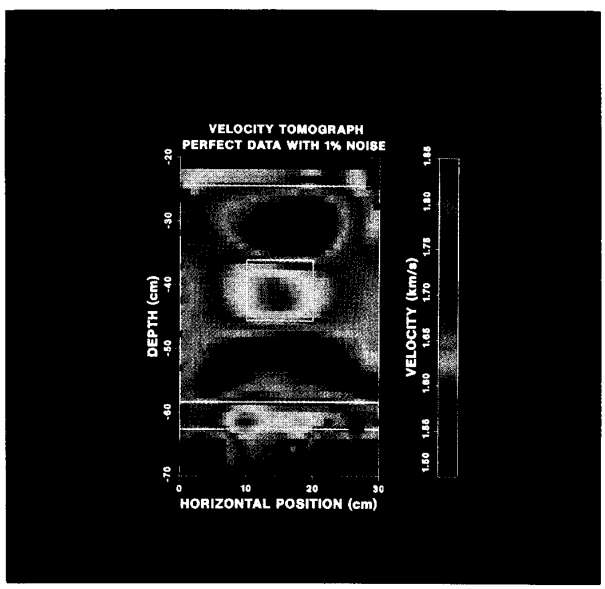

(c)

Fig. 10. (a) Velocity tomograph from laboratory data showing velocity structure of the region depicted in the overlay. (b) Velocity tomograph from computer-generated data. (c) Velocity tomograph from computer-generated data with 1% added noise. Velocities in km/s shown on color bar at right.

the image. The top and bottom of the container are distinct; however, the sides are somewhat blurred. The higher velocities for both sands observed in the tomography experiment compared to those obtained in the individual sand experiments are due in part to increases with velocity due to increased load. In addition, the straight ray assumption and the tendency for the tomography algorithm to distribute velocities along the entire ray paths also tend to increase velocities in the low-velocity regions.

The tomographic reconstruction of the perfect data shown in Fig. 10(b) demonstrates that most of the features seen in the laboratory data tomograph are visible, including the artifacts emanating from the water container. This observation indicates that the artifacts are due to the geometry of data collection and from using straight rays. Aside from the differences described above, the major difference between the theoretical and observed result is the noise present in the laboratory data tomograph. Noise results in minor variations of velocity from pixel to pixel in regions where no variations are expected, such as within the lower layer of RG sand. The tomograph obtained from the perfect data with noise (Fig. 10(c)) shows a degraded image from the perfect data alone. The absolute velocities are not identical, but many of the same features exist in the real data and the perfect data with noise. For example, the wings emanating from the water container and the lower velocities just below the top layer exist in the perfect data with noise.

Resolution limitations and artifacts result from the experimental geometry and the assumption of straight rays. The travel time data consisted of ray paths propagating at angles $\pm 50°$ from horizontal, and therefore no vertical paths were included. With such a measurement geometry horizontal boundaries will be imaged distinctly, while vertical boundaries will not. The addition of near-vertical ray paths would remove the nonuniqueness in the tomographic reconstruction, and thus limit distortion. This could be accomplished by placing transmitters or receivers along the surface between the boreholes. Finally, incorporating bending rays into the imaging algorithm may help decrease artifacts.

V. Conclusions

To our knowledge, this is the first time unconsolidated sediments have been imaged at high resolution in the laboratory using compressional waves. Toward the goal of developing a field tool for subsurface imaging, future experiments must focus on: 1) increasing distances between boreholes up to several meters, 2) incorporating horizontal stringers of transmitters or receivers along the surface to prevent horizontal smearing of velocity anomalies, 3) testing our ability to discern root densities within the soils, 4) testing the sensitivity of the technique under different levels of water saturation, 5) using shear wave travel times to produce tomographs of shear wave velocity structure, and 6) using amplitudes of compressional and shear waves to produce tomographs of Q structure. In view of the major problem of elastic wave attenuation within soils and sediments, considerable attention must be given to increasing the power of the transmitter and to improving coupling between the media and transmitters and receivers. Eventually, we hope to develop a field tool that can image sediments, fluids, soil, and root strata using the cross-borehole method.

VI. Summary

We used compressional wave cross-borehole tomography to image saturated, simulated layered sediments containing a low-velocity zone centered within the middle layer. The low-velocity zone was created using a water-filled container. The experiment was conducted in the laboratory using stringers of transmitter and receiver piezoelectric transducers. The transmitter and receiver stringers were spaced 30 cm apart. The stringers were novel: they were extremely efficient at coupling compressional waves into the sediments, while avoiding tube wave generation. The frequency of operation was 135 kHz, and wavelengths were approximately 1 cm in the sediments, with quality factors Q ranging from 11 to 25. Comparison of the tomograph from observed travel times and a tomograph generated from simulated data shows that we succeeded in imaging the water container, and to a lesser degree, the layers. This initial imaging experiment under laboratory conditions suggests that cross-borehole elastic wave tomography could be developed as a field tool for subsurface imaging.

Acknowledgment

The authors are grateful to T. Hakonson for suggesting this study, and for helpful support and discussions. S. Meadows made the original link between cross-borehole work in geologic and soil-sedimentary environments. They thank E. Stephani for help with transmitter and receiver design, and M. Gerety for suggesting improvements to the paper.

References

[1] W. M. Telford, L. P. Geldart, R. E. Sheriff, and D. A. Keys, *Applied Geophysics*. New York: Press Syndicate Univ. Cambridge, 1982.

[2] C. E. Glass, "Indirect rock mass investigations for optimizing borehole drilling programs, volume 1: Executive summary," NUREG/CR-3143, 1983.

[3] S. Crestana, S. Mascarenhas, and R. S. Pozzi-Mucelli, "Static and dynamic three-dimensional studies of water in soil using computer tomographic scanning," *Soil Sci.*, vol. 140, pp. 326-332, 1985.

[4] P. Daily, "Nuclear magnetic resonance imaging: An innovative method for the study of structure and function of plant roots," in *Meeting Summary: Innovation in Ecology: Technology and Theory*. Ecological Res. Div., DOE Office of Energy Res., 1987.

[5] N. Ricker, "The form and laws of propagation of seismic wavelets," *Geophys.*, vol. 18, pp. 10-40, 1953.

[6] F. J. McDonal *et al.*, "Attenuation of shear and compressional waves in Pierre shale," *Geophys.*, vol. 23, pp. 421-439, 1958.

[7] J. E. White and R. L. Sengbush, "Velocity measurements in near-surface formations," *Geophys.*, vol. 18, pp. 54-69, 1953.

[8] K. H. Stokoe and R. D. Woods, "*In-situ* shear wave velocity by crosshole method," *J. Soil Mech. Fond. Div.*, vol. 98, pp. 443-460, 1972.

[9] D. M. McCann, P. Grainger, and C. McCann, "Inter-borehole acoustics measurements and their use in engineering geology," *Geophys. Prospecting*, vol. 23, pp. 50-69, 1975.

[10] B. Auld, "Cross-hole and down-hole v_s by mechanical impulse," *J. Geotech. Eng. Div.*, vol. 103, pp. 1381-1398, 1975.
[11] R. J. Swain, "Bottom of San Francisco Bay evaluated for Trans-Bay Tube," *Civil Eng.*, vol. 11, pp. 66-67, 1960.
[12] R. Gordon, R. Bender, and G. T. Herman, "Algebraic reconstruction techniques (ART) for three-dimensional electron microscopy and X-ray photography," *J. Theoret. Biol.*, vol. 29, pp. 471-481, 1970.
[13] G. T. Herman, A. Lent, and S. W. Rowland, "ART: Mathematics and applications," *J. Theoret. Biol.*, vol. 42, pp. 1-32, 1973.
[14] M. Bois, M. LaPorte, M. Lavergne, and G. Thomas, "Well-to-well seismic measurements," *Geophys.*, vol. 37, pp. 471-480, 1972.
[15] I. M. Mason, "Algebraic reconstruction of a two-dimensional velocity inhomogeneity in the high Hazles seam of Thoresby colliery," *Geophys.*, vol. 46, pp. 298-308, 1981.
[16] M. Gustavsson, H. Israelson, S. Ivansson, P. Moren, and J. Pihl, "An experiment with the seismic crosshole method in an iron mine," *Geophys.: Leading Edge of Exploration*, vol. 3, pp. 143-145, 1984.
[17] M. C. Fehler and C. M. Pearson, "Cross-hole seismic surveys: Applications for studying subsurface fracture systems at a hot dry rock geothermal site," *Geophys.*, vol. 49, pp. 37-45, 1984.
[18] J. H. Justice *et al.*, "Acoustic tomography for monitoring enhanced oil recovery," *Geophys.: Leading Edge of Exploration*, vol. 8, pp. 12-19, 1989.
[19] J. Wong, P. Hurley, and G. F. West, "Crosshole audiofrequency seismology in granitic rocks using piezoelectric transducers as sources and detectors," *Geoexploration*, vol. 22, pp. 261-279, 1984.
[20] B. N. P. Paulsson, N. G. W. Cook, and T. V. McEvilly, "Elastic-wave velocities and attenuation in an underground granitic repository for nuclear waste," *Geophys.*, vol. 50, pp. 551-570, 1985.
[21] G. Sattel and C. Gelbke, "Non-destructive rock testing with seismic cross-hole tomography," in *SEG 1987 Ann. Meet., Expanded Abstr.*, 1987, pp. 845-847.
[22] J. E. Peterson, B. N. P. Paulsson, and T. V. McEvilly, "Applications of algebraic reconstruction techniques to crosshole seismic data," *Geophys.*, vol. 50, pp. 1566-1580, 1985.
[23] G. A. McMechan, "Seismic tomography in boreholes," *Geophys. J. Roy. Astron. Soc.*, vol. 74, pp. 601-612, 1983.
[24] W. Menke, "The resolving power of cross-borehole tomography," *Geophys. Res. Lett.*, vol. 11, pp. 105-108, 1984.
[25] A. L. Ramirez, "Reconstruction of simulated lineaments using geophysical tomography," *Int. J. Rock Mech., Mineral Sci., Geomech. Abstr.*, vol. 23, pp. 157-163, 1986.
[26] S. Ivansson, "A study of methods for tomographic velocity estimation in the presence of low-velocity zones," *Geophys.*, vol. 50, pp. 969-988, 1985.
[27] W. S. Phillips, P. A. Johnson, and J. N. Albright, "Cross-hole tomography at Rifle, Colorado," in *SEG 56th Ann. Meet., Expanded Abstr.*, 1986, pp. 228-230.
[28] M. N. Toksoz and R. R. Stewart, *Vertical Seismic Profiling—Advance Concepts*. London: Geophysical Press, 1984.
[29] D. H. Johnston and M. N. Toksoz, *Seismic Wave Attenuation (Introduction)* (Soc. Exploration Geophysicists Geophys. Reprint Series 2). Tulsa, OK: SEGG, 1981.
[30] K. A. Dines and R. J. Lytle, "Computerized geophysical tomography," *Proc. IEEE*, vol. 67, pp. 1065-1073, 1979.
[31] R. H. Wilkens, G. Simmons, T. M. Wissler, and L. Caruso, "The physical properties of a set of sandstones—Part III. The effects of fine-grained pore-filling material on compressional wave velocity," *Int. J. Rock Mech. Mineral Sci., Geomech. Abstr.*, vol. 23, pp. 313-325, 1986.
[32] E. L. Hamilton, "Compressional wave attenuation in marine sediments," *Geophys.*, vol. 37, pp. 620-646, 1972.

*

Timothy H. Larkin received the B.S.M.E. degree from New Mexico State University, Las Cruces, in 1986. On the undergraduate student program, he worked on the computer analysis and testing of downhole tools used in the Hot Dry Rock Program at the Los Alamos National Laboratory (LANL), Los Alamos, NM. Next, with the Associated Western University Assistantship Program, he worked on a research team to design and test an elastic wave device for remote sensing of soils at LANL. As a student on the Graduate Research Assistantship (GRA) Program at LANL, he worked on a research team to thermally analyze high-power microwave transistors. Presently, he is working in the area of thermal-structual design and analysis of RF cavities and magnets. His research interests are in computer design and analysis.

*

Paul A. Johnson received the B.S. degree in geology from the University of New Mexico, Albuquerque, in 1978, and the M.S. degree in geophysics from the University of Arizona, Tucson, in 1982.

He is presently employed as a Staff Member at the Los Alamos National Laboratory, Los Alamos, NM. His present research interests include seismic imaging and nonlinear elastic wave studies.

*

Paul M. Rich received the Ph.D. degree from Harvard University, Cambridge, MA, in the Department of Organismic and Evolutionary Biology.

Subsequently, he was a Postdoctoral Fellow in the Environmental Sciences Group at Los Alamos National Laboratory, and later at Stanford University. He is currently a Research Associate in the Department of Biological Sciences at Stanford University, Palo Alto, CA. His research interests include relations between plant form and function, plant canopy structure, and tropical forest dynamics. He has special research interest in digital image analysis techniques and the application of close-range remote sensing to study ecological systems.

*

Greg Eischeid is currently an undergraduate student at the University of New Mexico, Albuquerque, and a participant in the cooperative education program at the Los Alamos National Laboratory, Los Alamos, NM. He will receive the Bachelor of University Studies degree in December 1990, concentrating in mathematics and engineering. His research interests are in signal processing and numerical computing.

*

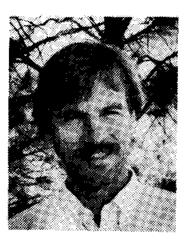

W. Scott Phillips received the B.A. degree in geophysics from the University of California at Berkeley in 1979, and the Ph.D. degree in geophysics from the Massachusetts Institute of Technology, Cambridge, in 1985.

He is presently employed as a Consultant at the Los Alamos National Laboratory, Los Alamos, NM. His research interests include seismic imaging and local earthquake seismology.